

# Magnetic Induction in Convecting Galilean Oceans

S. D. Vance<sup>1</sup>, B. G. Bills<sup>1</sup>, C. J. Cochrane<sup>1</sup>, K. M. Soderlund<sup>2</sup>,  
N. Gómez-Pérez<sup>3</sup>, M. J. Styczinski<sup>4</sup>, and C. Paty<sup>5</sup>

<sup>1</sup>Jet Propulsion Laboratory, California Institute of Technology, Pasadena, USA

<sup>2</sup>Institute for Geophysics, John A. & Katherine G. Jackson School of Geosciences, The University of  
Texas at Austin, USA

<sup>3</sup>British Geological Survey, Edinburgh, UK

<sup>4</sup>Dept. of Physics, University of Washington, Seattle, USA

<sup>5</sup>Dept. of Earth Sciences, University of Oregon, Eugene, USA

## Key Points:

- Diffusive induction accounting for adiabatic ocean temperatures is distinct in phase and amplitude from induction based on electrical conductivity at the ice-ocean interface
- Based on turbulent global convection models, oceanic flows may generate induced magnetic fields observable by planned spacecraft missions
- Determining ocean composition from magnetic induction requires additional thermodynamic and electrical conductivity data

arXiv:2002.01636v3 [physics.geo-ph] 6 Mar 2020

**Abstract**

To date, analyses of magnetic induction in putative oceans in Jupiter’s large icy moons have assumed uniform conductivity in the modeled oceans. However, the phase and amplitude response of the induced fields will be influenced by the increasing electrical conductivity along oceans’ convective adiabatic temperature profiles. Here, we examine the amplitudes and phase lags for magnetic diffusion in modeled oceans of Europa, Ganymede, and Callisto. We restrict our analysis to spherically symmetric configurations, treating interior structures based on self-consistent thermodynamics, accounting for variations in electrical conductivity with depth in convective oceans (Vance et al., 2018). The numerical approach considers tens of radial layers. The induction response of the adiabatic conductivity profile differs from that of an ocean with uniform conductivity set to that at the ice-ocean interface, or to the mean value of the adiabatic profile, by more than 10% in many cases. We compare these modeled signals with magnetic fields induced by oceanic fluid motions that might be used to measure oceanic flows (e.g., Chave, 1983; Tyler, 2011; Minami, 2017). For turbulent convection (, Soderlund et al.2014), we find that these signals can dominate induction signal at low latitudes, underscoring the need for spatial coverage in magnetic investigations. Based on end-member ocean compositions (Zolotov, 2008; Zolotov & Kargel, 2009), we quantify the residual magnetic induction signals that might be used to infer the oxidation state of Europa’s ocean and to investigate stable liquids under high-pressure ices in Ganymede and Callisto. Fully exploring this parameter space for the sake of planned missions requires electrical conductivity measurements in fluids at low temperature and to high salinity and pressure.

**1 Introduction**

The jovian system is of particular interest for studying magnetic induction in icy ocean worlds. Jupiter has a strong magnetic field whose dipole axis is tilted  $9.5^\circ$  with respect to its rotation axis (Acuna & Ness, 1976), while the orbits of the Galilean moons lie very nearly in the equatorial plane of Jupiter. This means that Jupiter’s magnetic field varies in time at the orbital positions of the satellites. Also, the outer layers of the satellites themselves are believed to consist mainly of water ice at the surface, underlain by salty oceans. Brines are good conductors, while ice is a significant insulator.

Magnetic induction from Jupiter’s diurnal signal sensed by the *Galileo* mission provides the most compelling direct observational evidence for the existence of oceans within Europa and Ganymede (Saur et al., 1998; Khurana et al., 1998; Kivelson et al., 2000; Schilling et al., 2007; Hand & Chyba, 2007; Khurana et al., 2009). The case has also been made for an induction response from an ocean in Callisto (Zimmer et al., 2000), but this interpretation is clouded by possible ionospheric interference (Liuzzo et al., 2015; Hartkorn & Saur, 2017).

Longer period signals penetrate more deeply, as penetration of the magnetic field into the interior is a diffusive process. It is convenient that the skin depths at the dominant periods of variation experienced by Europa, Ganymede, and Callisto are comparable to the expected ocean depths, which makes it possible to probe the properties of their oceans using magnetic induction. The spectrum of frequencies driving induced magnetic responses includes not just the orbits of the Galilean satellites and the rotation of Jupiter’s tilted dipole field, but also their harmonics and natural oscillations (Saur et al., 2009; Seufert et al., 2011). Electrical conductivity structure within the subsurface oceans—for example, from convective adiabatic temperature gradients (Vance et al., 2018) and stratification (Vance & Goodman, 2009a)—will respond at these frequencies.

Further variations in the magnetic fields arise from the motion of the moons about Jupiter. Perturbations to the orbits of the moons arise from multiple sources, including the oblate figure of Jupiter, gravitational interactions with the other satellites, and even from Saturn and the Sun (Lieske, 1998; Lainey et al., 2006).

Here, we examine the amplitudes and phase lags for magnetic diffusion in modeled oceans of Europa, Ganymede, and Callisto. We restrict our analysis to spherically symmetric configurations, treating interior structures based on self-consistent thermodynamics, which account for variations in electrical conductivity with depth in convective oceans (Vance et al., 2018). In addition, we consider the generation of induced magnetic fields by oceanic fluid motions that may bias the interpretation of a satellite’s magnetic behavior if not accommodated and which, more optimistically, might be used to probe the ocean flows directly (e.g., Chave, 1983; Tyler, 2011; Minami, 2017). Based on end-member ocean compositions (Zolotov, 2008; Zolotov & Kargel, 2009), we demonstrate the possibilities for using magnetic induction to infer the oxidation state of Europa’s ocean and to identify stable liquid layers under high-pressure ices in Ganymede and Callisto.

In Section 2 we describe a numerical method for computing the induction response. Section 3 examines the diffusive induction response of Jupiter’s ocean moons, first describing the frequency content of temporal variations in Jupiter’s field in the reference frames of the Galilean moons (S 3.1), then the interior structure models that include layered electrical conductivity consistent with the modeled compositions (S 3.2). In Section 3.3, we detail the corresponding amplitude and phase responses of the diffusive magnetic induction, and finally in Section 3.4, we compare the diffusive fields to the field imposed by Jupiter. Section 4 describes simulations of oceanic flows (S 4.1) and resulting magnetic induction (S 4.2) that adds to the diffusive component. Section 5 describes the prospects for detecting these different signals.

## 2 Induction Response Model

We are interested in the magnetic fields induced within a spherically symmetric body, in which electrical conductivity is a piece-wise constant function of distance from the center. We thus assume bounding radii

$$\{r_1, r_2, r_3, \dots, r_m\} \quad (1)$$

where

$$r_m = R \quad (2)$$

is the outer radius of the spherical body.

The corresponding conductivity values are

$$\{\sigma_1, \sigma_2, \sigma_3, \dots, \sigma_m\} \quad (3)$$

We also assume that there is an imposed external magnetic potential, represented by a sum of terms, each of which has the form

$$\Phi[r, \theta, \phi, t] = R B_e \left(\frac{r}{R}\right)^n S_{n,m}[\theta, \phi] \exp[-i \omega t] \quad (4)$$

where  $\{r, \theta, \phi\}$  are spherical coordinates ( $r$  is radius,  $\theta$  is colatitude, and  $\phi$  is longitude) of the field point,  $B_e$  is a scale factor,  $S_{n,m}[\theta, \phi]$  is a surface spherical harmonic function of degree  $n$  and order  $m$ , while  $t$  is time and  $\omega$  is the frequency of oscillation of the imposed potential.

Within each layer, the magnetic field vector  $B$  must satisfy the differential equation

$$\nabla^2 B = -k^2 B \quad (5)$$

where  $k$  is a scalar wavenumber given by

$$k^2 = i \omega \mu_0 \sigma \quad (6)$$

where  $\omega$  is frequency,  $\sigma$  is electrical conductivity, and the magnetic constant (permeability of free space) is given by

$$\mu_0 = 4\pi \times 10^{-7} N/A^2 \quad (7)$$

with units  $N$  and  $A$  being Newton and Ampere.

## 2.1 Radial Basis Functions

The poloidal component of the magnetic field inside the body is given by sums of terms with the forms

$$B_r[r, \theta, \phi, t] = \frac{C}{r} (F[r]) n(n+1) S_{n,m}[\theta, \phi] \exp[-i \omega t] \quad (8)$$

$$B_\theta[r, \theta, \phi, t] = \frac{C}{r} \left( \frac{d r F[r]}{dr} \right) \frac{d S_{n,m}[\theta, \phi]}{d\theta} \exp[-i \omega t] \quad (9)$$

$$B_\phi[r, \theta, \phi, t] = \frac{C}{r \sin[\theta]} \left( \frac{d r F[r]}{dr} \right) \frac{d S_{n,m}[\theta, \phi]}{d\phi} \exp[-i \omega t] \quad (10)$$

where  $C$  is a constant, and  $F[r]$  is a function of radius, which we need to determine.

Applying separation of variables to the governing differential equation (5), one finds that the radial factor  $F[r]$  in the solution must satisfy the ordinary differential equation

$$\frac{d^2 F}{dr^2} + \left( \frac{2}{r} \right) \frac{dF}{dr} + \left( k^2 - \frac{n(n+1)}{r^2} \right) F = 0 \quad (11)$$

This is a second order equation having two solutions:

$$F_n^+[r] = j_n[k r] \quad (12)$$

$$F_n^-[r] = y_n[k r] \quad (13)$$

where  $j_n[x]$  is a spherical Bessel function of the first kind of order  $n$ , and argument  $x$ , and  $y_n[x]$  is a spherical Bessel function of the second kind.

It will also be convenient to define another set of related functions

$$\begin{aligned} G_n^+[r] &= \frac{d}{dr} (r F_n^+[r]) \\ &= (n+1) j_n[k r] - (k r) j_{n+1}[k r] \end{aligned} \quad (14)$$

and

$$\begin{aligned} G_n^-[r] &= \frac{d}{dr} (r F_n^-[r]) \\ &= (n+1) y_n[k r] - (k r) y_{n+1}[k r] \end{aligned} \quad (15)$$

In the magnetic induction problem, as applied to the Galilean satellites, the only case of interest is for an imposed dipole field, where  $n = 1$ . In that case, the radial basis functions for the radial component of the field, are

$$\begin{aligned} F_1^+[k r] &= j_1[k r] \\ &= \frac{\sin[k r] - (k r) \cos[k r]}{(k r)^2} \end{aligned} \quad (16)$$

and

$$\begin{aligned} F_1^- [k r] &= y_1 [k r] \\ &= \frac{-\cos[k r] - (k r) \sin[k r]}{(k r)^2} \end{aligned} \quad (17)$$

In similar fashion, the radial basis functions for the transverse components are

$$\begin{aligned} G_1^+ [k r] &= 2 j_1 [k r] - (k r) j_2 [k r] \\ &= \frac{(k r) \cos[k r] - (1 - k^2 r^2) \sin[k r]}{(k r)^2} \end{aligned} \quad (18)$$

and

$$\begin{aligned} G_1^- [k r] &= 2 y_1 [k r] - (k r) y_2 [k r] \\ &= \frac{(k r) \sin[k r] + (1 - k^2 r^2) \cos[k r]}{(k r)^2} \end{aligned} \quad (19)$$

In both cases, the latter form is singular at the origin ( $r = 0$ ), so in the innermost spherical layer, we only use  $F^+ [k r]$  and  $G^+ [k r]$ . In other layers, we use linear combinations of  $F^+$  and  $F^-$  and linear combinations of  $G^+$  and  $G^-$ .

## 2.2 Internal Boundary Conditions

The resulting piece-wise-defined radial functions characterize the radial part of the magnetic field. The radial component has the form

$$F[r] = \begin{cases} c_1 F^+ [k_1 r] & \text{if } 0 < r \leq r_1 \\ c_2 F^+ [k_2 r] + d_2 F^- [k_2 r] & \text{if } r_1 < r \leq r_2 \\ c_3 F^+ [k_3 r] + d_3 F^- [k_3 r] & \text{if } r_2 < r \leq r_3 \\ \dots & \dots \\ c_m F^+ [k_m r] + d_m F^- [k_m r] & \text{if } r_{m-1} < r \leq r_m \end{cases} \quad (20)$$

The transverse components yield similar structure, but with  $G$  replacing  $F$ .

The constants  $c_j$  and  $d_j$  are determined by continuity of radial ( $r$ ) and transverse ( $\theta, \phi$ ) components of the magnetic field across the boundaries. For each internal boundary, it must hold that

$$\begin{aligned} F[r_j] &= c_j F^+ [k_j r_j] + d_j F^- [k_j r_j] \\ &= c_{j+1} F^+ [k_{j+1} r_j] + d_{j+1} F^- [k_{j+1} r_j] \end{aligned} \quad (21)$$

to ensure continuity of the radial component of the magnetic field, and likewise for  $G$  to ensure continuity of the transverse components. These continuity constraints yield two equations at each internal boundary, from which we can determine the layer coefficients.

The internal boundary conditions are only part of the story. In a model with  $m$  layers, we have  $2m - 1$  coefficients to determine (recall that  $d_1 = 0$ , to avoid singular behavior at the origin), but only  $m - 1$  internal boundaries, and thus only  $2m - 2$  constraints. The external boundary condition provides the additional information to make the problem evenly determined.

Even without the external boundary condition, a provisional solution is obtained by setting  $c_1 = 1$  and using the internal boundary constraints to determine the other coefficient values. Using notation similar to that of Parkinson (1983, page 314), we can write a recursion relation that transforms the coefficients in the  $j$ th layer into those for the layer above it

$$\begin{bmatrix} c_{j+1} \\ d_{j+1} \end{bmatrix} = T_j [k_j, k_{j+1}, r_j] \cdot \begin{bmatrix} c_j \\ d_j \end{bmatrix} \quad (22)$$

where the transformation matrix has elements

$$T_j[k_j, k_{j+1}, r_j] = \frac{1}{\alpha_j} \begin{bmatrix} \beta_j & \gamma_j \\ \delta_j & \varepsilon_j \end{bmatrix} \quad (23)$$

with

$$\alpha_j = F^+[k_{j+1} \ r_j] * G^- [k_{j+1} \ r_j] - F^- [k_{j+1} \ r_j] * G^+ [k_{j+1} \ r_j] \quad (24)$$

which is a function of the conductivity in the layer above the boundary only. The other elements depend on the conductivities on both sides of the boundary

$$\beta_j = F^+[k_j \ r_j] * G^- [k_{j+1} \ r_j] - F^- [k_{j+1} \ r_j] * G^+ [k_j \ r_j] \quad (25)$$

$$\gamma_j = F^- [k_j \ r_j] * G^- [k_{j+1} \ r_j] - F^- [k_{j+1} \ r_j] * G^- [k_j \ r_j] \quad (26)$$

and

$$\delta_j = F^+[k_{j+1} \ r_j] * G^+ [k_j \ r_j] - F^+ [k_j \ r_j] * G^+ [k_{j+1} \ r_j] \quad (27)$$

$$\varepsilon_j = F^+ [k_{j+1} \ r_j] * G^- [k_j \ r_j] - F^- [k_j \ r_j] * G^+ [k_{j+1} \ r_j] \quad (28)$$

We thus start in the central spherical layer, with  $c_1 = 1$  and  $d_1 = 0$ , and then propagate upward through the stack of layers until we have the coefficients in each of the  $m$  layers. This set of layer coefficients, with the radial basis functions, yields structures as given in equations (22) and (23).

### 2.3 External Boundary Conditions

The final step is matching the external surface boundary condition. Outside the sphere, the magnetic field is represented by a scalar potential which is the sum of an imposed external contribution and an induced internal contribution. That sum has spatial dependence given by the form

$$\Phi[r, \theta, \phi] = R \left( B_e \left( \frac{r}{R} \right)^n + B_i \left( \frac{R}{r} \right)^{n+1} \right) S_n[\theta, \phi] \quad (29)$$

We have dropped the subscript  $m$  from  $S_{n,m}$  because a suitable choice of axes results in  $m = 0$  for both external and internal fields for the case of spherical symmetry we consider here. The vector field is obtained from the potential via

$$B = -\nabla\Phi \quad (30)$$

The radial component of the vector field, evaluated at the surface ( $r = R$ ), is

$$B_r = -(n B_e - (n + 1)B_i) S_n[\theta, \phi] \quad (31)$$

and the tangential components are

$$B_\theta = -(B_e + B_i) \frac{\partial S_n[\theta, \phi]}{\partial \theta} \quad (32)$$

and

$$B_\phi = -(B_e + B_i) \frac{1}{\sin[\theta]} \frac{\partial S_n[\theta, \phi]}{\partial \phi} \quad (33)$$

Matching these with the corresponding interior components, as given in equations (8), (9), and (10), but evaluated at the top of the upper-most layer, we obtain

$$-(n B_e - (n + 1) B_i)R = n (n + 1) (c_m F^+[k_m \ R] + d_m F^- [k_m \ R]) \quad (34)$$

and

$$-(B_e + B_i)R = (c_m G^+[k_m \ R] + d_m G^- [k_m \ R]) \quad (35)$$

From these two equations, we can first solve for  $B_e$  and  $B_i$ . The result is

$$\widehat{B}_e = \frac{-1}{R(2n+1)} (c_m A_m + d_m B_m) \quad (36)$$

$$\widehat{B}_i = \frac{1}{R(2n+1)} (c_m C_m + d_m D_m) \quad (37)$$

where we introduce  $\widehat{B}_e$  and  $\widehat{B}_i$  to distinguish solutions in terms of internal properties from the external and induced magnetic moments. We also define the parameters  $A_m$ ,  $B_m$ ,  $C_m$ , and  $D_m$  by

$$\begin{aligned} A_m &= (n+1) (n F^+[k_m R] + G^+[k_m R]) \\ B_m &= (n+1) (n F^-[k_m R] + G^-[k_m R]) \end{aligned} \quad (38)$$

and

$$\begin{aligned} C_m &= n ((n+1) F^+[k_m R] - G^+[k_m R]) \\ D_m &= n ((n+1) F^-[k_m R] - G^-[k_m R]) \end{aligned} \quad (39)$$

As previously noted, choice of  $c_1 = 1$  permits solution of layer coefficients  $c_j$  and  $d_j$  relative to each other with only knowledge of the interior properties. We can then solve for  $\widehat{B}_e$  and  $\widehat{B}_i$  in terms of the interior structure quantities  $k_j$  and  $r_j$ . We can then conveniently relate this to the magnetic field that will be induced from the conducting body for a given external field  $B_e^*$  by introducing a scale factor:

$$S = \frac{B_e^*}{\widehat{B}_e} \quad (40)$$

Choosing a normalized value of

$$B_e^* = 1 \quad (41)$$

means that physically correct layer coefficients may be determined by multiplying the magnitude of the applied external field to the coefficients  $c_j^*$  and  $d_j^*$ , obtained from

$$\begin{bmatrix} c_j^* \\ d_j^* \end{bmatrix} = S \begin{bmatrix} c_j \\ d_j \end{bmatrix} \quad (42)$$

For an applied external field  $B_e^*$  in real units, the physical magnetic field within each layer is then given by

$$\begin{aligned} B_{r,j}[r, \theta, \phi, t] &= \frac{B_e^*}{r} (c_j^* F^+[k_j r] + d_j^* F^-[k_j r]) n(n+1) S_n[\theta, \phi] \exp[-i \omega t] \\ B_{\theta,j}[r, \theta, \phi, t] &= \frac{B_e^*}{r} (c_j^* G^+[k_j r] + d_j^* G^-[k_j r]) \frac{dS_n[\theta, \phi]}{d\theta} \exp[-i \omega t] \\ B_{\phi,j}[r, \theta, \phi, t] &= \frac{B_e^*}{r \sin[\theta]} (c_j^* G^+[k_j r] + d_j^* G^-[k_j r]) \frac{dS_n[\theta, \phi]}{d\phi} \exp[-i \omega t] \end{aligned} \quad (43)$$

The ratio of internal and external field strengths at the exterior surface is given from equations (36) and (37) via

$$Q \equiv \frac{\widehat{B}_i}{\widehat{B}_e} = -\frac{c_m^* C_m + d_m^* D_m}{c_m^* A_m + d_m^* B_m} \quad (44)$$

In Zimmer et al. (2000) and Khurana et al. (2009), this complex ratio is written as the product of a real magnitude and a phase shift:

$$Q = A^* \exp[i \gamma^*] \quad (45)$$

where  $A^*$  is a positive real number representing amplitude and  $\gamma^*$  is a real number representing the phase of the induced field relative to the imposed field.

In the aforementioned previous work, an explicit formula is given for the result from a 3-layer model, in which the conductivities in the innermost ( $j = 1$ ) and outermost ( $j = 3$ ) layers are zero, and the middle layer (intended to represent a salty ocean in Europa) has a finite conductivity. In this model, there are essentially four free parameters—3 bounding radii ( $r_1, r_2, r_3$ ) and a middle layer conductivity ( $\sigma_2$ )—that determine the critical wavenumber ( $k_2$ ). We refer to this model as the ocean-only model.

In our notation, the resulting ratio  $Q$  for the ocean-only model is

$$Q = \frac{-n}{n+1} \frac{j_{n+1}[k_2 r_1] * y_{n+1}[k_2 r_2] - j_{n+1}[k_2 r_2] * y_{n+1}[k_2 r_1]}{j_{n+1}[k_2 r_1] * y_{n-1}[k_2 r_2] - j_{n-1}[k_2 r_2] * y_{n+1}[k_2 r_1]} \quad (46)$$

Because we know the complex phase of the wavenumber  $k$ , we can use properties of Bessel functions to solve for the amplitude and phase for the induced magnetic field. We defined  $k^2 = i\omega\mu\sigma$  (Eq. 6), so  $k = \exp[i\pi/4]\sqrt{\omega\mu\sigma}$ . The (real) magnitude of  $k$  is  $|k| = \sqrt{\omega\mu\sigma}$ , and all layers will have the same complex phase  $\pi/4$ . We can therefore express the wavenumber for each layer as

$$k_j = \kappa_j \exp[i\pi/4], \quad \kappa_j = \sqrt{\omega\mu_j\sigma_j} \quad (47)$$

When  $\kappa_2 r_2$  is large,  $j_{n+1}[\kappa_2 r_2] = -j_{n-1}[\kappa_2 r_2]$  and  $y_{n+1}[\kappa_2 r_2] = -y_{n-1}[\kappa_2 r_2]$ . We can make use of these relations to note that the amplitude and phase for the induced magnetic field for a perfectly conducting sphere of radius  $r_2$  will be  $n/(n+1)$  and 0, respectively. Thus, we can also define an amplitude and phase for the induction response relative to those for a perfectly conducting sphere of radius  $R$ :

$$A = A^* \frac{n+1}{n} \left(\frac{r_2}{R}\right)^3, \quad \gamma = \gamma^* \quad (48)$$

A perfectly conducting sphere of radius  $R$  therefore has a relative amplitude of  $A = 1$  and  $\gamma = 0$ .

### 3 Diffusive Induction in Jupiter’s Ocean Moons

#### 3.1 Spectral Content of the Imposed Magnetic Field Variations

Temporal variations in the magnetic field occur in the reference frames of Jupiter’s satellites. Figure 1 shows the strongest components, arising from the orbital and synodic periods and their harmonics. Seufert et al. (2011) determined the frequency spectra for the time-varying magnetic perturbations applied to each of the four Galilean moons based on the VIP4 model of J. Connerney et al. (1998) and the Jovian current sheet model of Khurana (1997). Seufert et al. (2011) also examined the frequency spectra of magnetic perturbations from dynamic migration of the Jovian magnetopause based on solar wind data from the Ulysses spacecraft, which we do not consider here.

To calculate the frequencies, we first compute the magnetic field using the JRM09 Jupiter field model accounting for Juno measurements (J. E. P. Connerney et al., 2018) and using the plasma sheet model from Khurana (1997). We then compute the field at the orbital positions of the moons using the most recent and up-to-date NAIF-produced spice kernels and three years of data covering the duration of the Europa Clipper mission (tour 17F12v2). Finally, we compute the Fourier transform of the entire data sets to determine the induction frequencies.

The temporal variations in imposed magnetic field at each satellite depend on the orbits of the satellites and the magnetic field of Jupiter. To find them, we compute Jupiter’s magnetic field in a Jupiter-centered coordinate system from a spherical



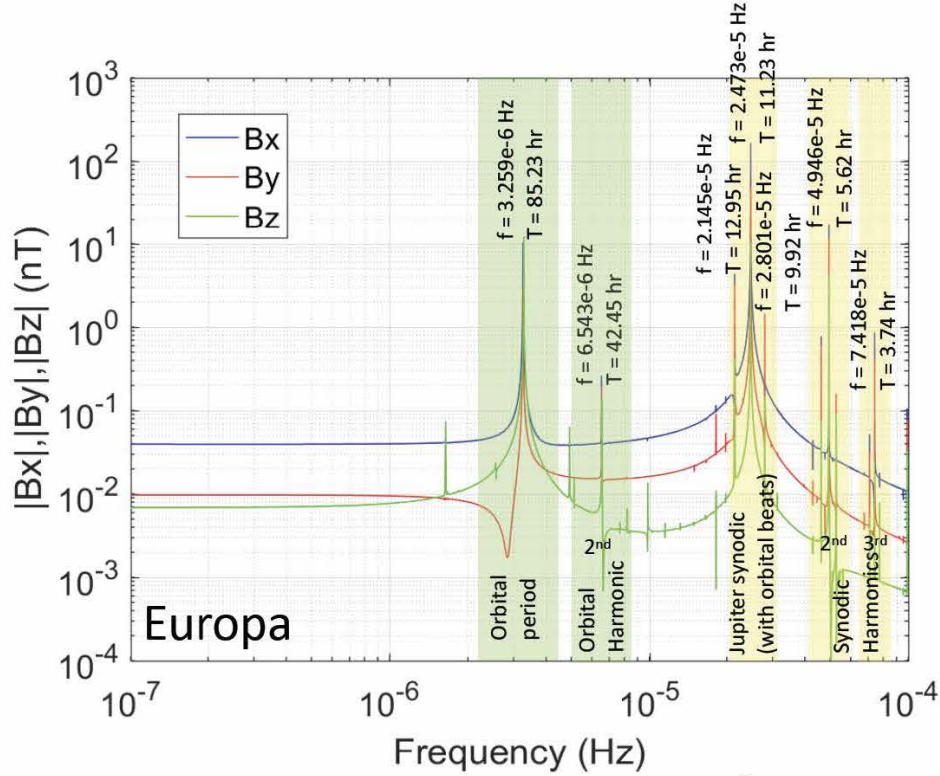


Figure 1: Europa: Variations in orbital parameters over time introduce magnetic fluctuations at multiple frequencies beyond the Jupiter rotation and satellite orbital frequencies. The different vector components contain unique information at multiple frequencies resulting from the harmonics and beats of the orbital and rotational oscillations.

harmonic series representation of the magnetic potential, which is a variant of Eq. 4:

$$\Phi[r, \theta, \phi] = R \sum_{n=1}^{n+1} \left(\frac{R}{r}\right)^{n+1} \sum_{m=0}^n P_{n,m}[\sin[\theta]] (g_{n,m} \cos[m\phi] + h_{n,m} \sin[m\phi]). \quad (49)$$

The magnetic field vector is the negative gradient of the scalar potential

$$B = -\nabla\Phi \quad (50)$$

$$= -\left\{ \frac{\partial\Phi}{\partial x}, \frac{\partial\Phi}{\partial y}, \frac{\partial\Phi}{\partial z} \right\} \quad (51)$$

The mean radius is  $R = 71,492$  km. The rotation rate of Jupiter, as defined in the System III longitude (Seidelmann & Divine, 1977), is  $\omega = 870.536^\circ/\text{day}$ .

### 3.2 Electrical Conductivity in Adiabatic Galilean Oceans

Fluid temperature, pressure, and salt content determine the electrical conductivity of an aqueous solution, and thus dictate the magnetic induction responses of the Galilean oceans. The amplitude and phase of the magnetic fields induced by the oceans depend on the conductive properties of the oceans, which are influenced by the composition of the dissolved salts. With sufficient prior knowledge of the ice thickness and hints to the ocean's composition—for example, from geological and compositional measurements by the Europa Clipper (Buffington et al., 2017)—magnetic induction

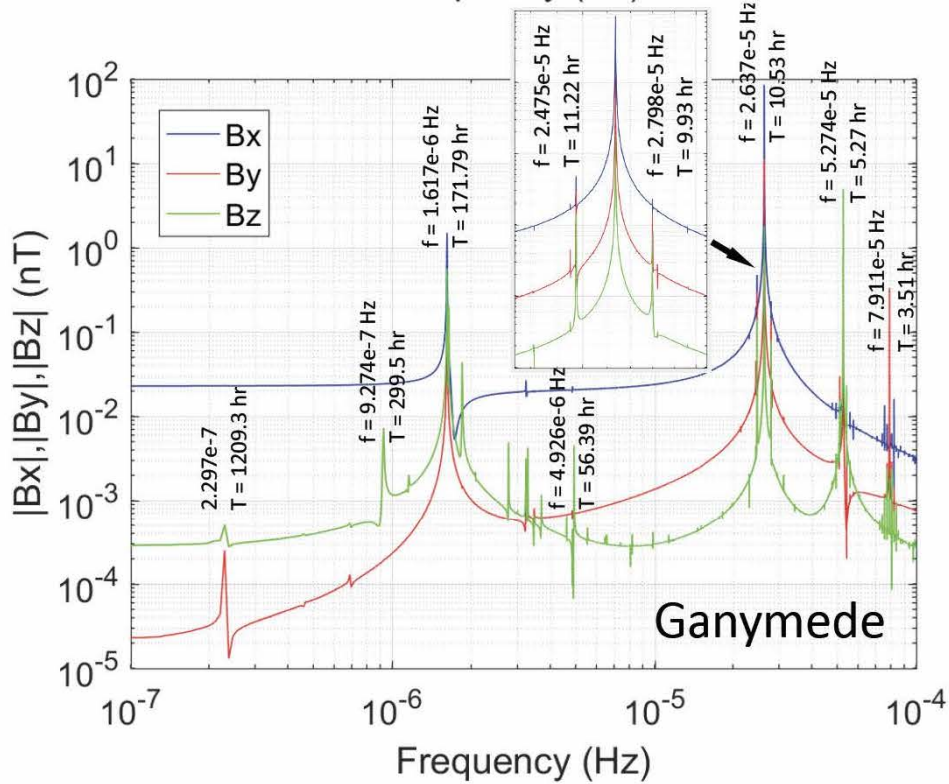


Figure 2: Ganymede: Variations in orbital parameters over time introduce magnetic fluctuations at multiple frequencies beyond the Jupiter rotation and satellite orbital frequencies.

studies can provide information on the amounts and compositions of the salts that link to global thermal and geochemical processes. On Europa, the flux of surface-generated oxygen to the ocean may have created oxidizing (acidic) conditions (Hand & Chyba, 2007; Pasek & Greenberg, 2012; Vance et al., 2016) permitting the presence of dissolved  $\text{MgSO}_4$  in addition to  $\text{NaCl}$  (Zolotov, 2008; Zolotov & Kargel, 2009).

Depth-dependent electrical conductivity can arise from melting or freezing at the ice–ocean interface, and from dissolution and precipitation within the ocean or at the water–rock interface. Even for oceans with uniform salinity, as is typically assumed, conductivity will increase with depth along the ocean’s convective adiabatic profile because the greater temperature and pressure increase the electrical conductivity. Figure 4 depicts this variation for Europa and Ganymede, based on forward models of Vance et al. (2018) that use available thermodynamic and geophysical data to explore the influences of the ocean, rock layer, and any metallic core on the radial structures of known icy ocean worlds. For each ocean, we consider a nominal 10 wt%  $\text{MgSO}_4$  salinity, as investigated in previous work. The published equation of state and electrical conductivity data are adequate for the pressures in the largest moon, Ganymede, up to 1.6 GPa (Vance et al., 2018). The pressure conditions in Europa’s ocean are low enough ( $< 200$  MPa) that the equation of state for seawater (McDougall & Barker, 2011) provides plausible values of conductivity for salinity of 35 ppt less. For Europa, the respective radial models of electrical conductivity for oceans containing seawater and  $\text{MgSO}_4$  are consistent with compositions linked to chemically reducing and oxidizing model oceans cited above.

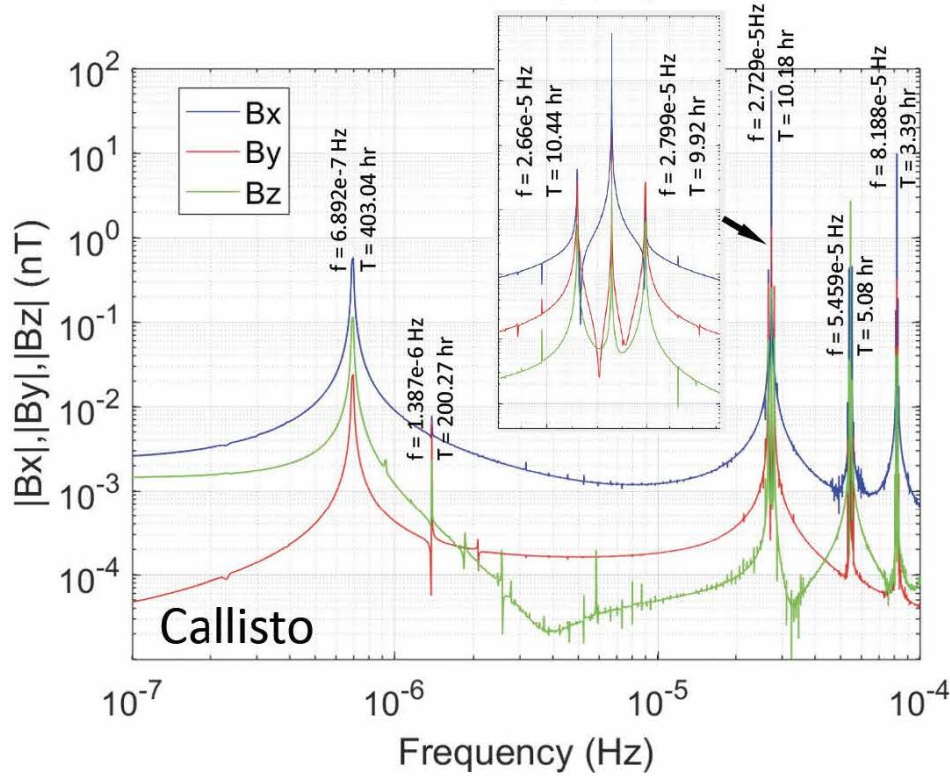


Figure 3: Callisto: Variations in orbital parameters over time introduce magnetic fluctuations at multiple frequencies beyond the Jupiter rotation and satellite orbital frequencies.

Radial conductivity profiles for Europa (Fig. 4; top) illustrate the coupling to temperature and composition. We consider ice thicknesses of 5 and 30 km (magenta and blue curves, respectively) as representative extremes. Seawater (dot-dashed lines), though less concentrated than the modeled composition of  $\text{MgSO}_4$  (dashed lines), has a stronger melting point suppression, leading to an overall colder ocean for the same thickness of ice. Adiabats for pure water (solid lines) are shown for comparison. The lower temperature for seawater combines with the different electrical conductivity for the different dissolved ions to create distinct profiles unique to ocean composition and ice thickness (upper right).

Larger Ganymede (Fig. 4; bottom) also has distinct conductivity profiles for both ice thickness and ocean composition. They reveal an additional nuance to deep planetary oceans that can influence the induction response. Although electrical conductivity generally increases with depth, it begins to decrease at the greatest depths for the warm Ganymede ocean (right-most curve). This inflection occurs because the ocean achieves GPa+ pressures, at which the packing of water molecules begins to inhibit the charge exchange of the dissolved ions (Schmidt & Manning, 2017).

Dense brines may also reside at the base of the high-pressure ices on Ganymede, and even between them (Journaux et al., 2013, 2017; S. Vance et al., 2014; Vance et al., 2018). Although more detailed modeling of the coupled geochemical and geodynamic regimes is needed, this scenario seems consistent with recent simulations of two-phase convection in high-pressure ices (Choblet et al., 2017). These simulations imply that fluids should occur at the water-rock interface through long periods of the evolution of even of large icy world containing high-pressure ices. If such a fluid layer exists

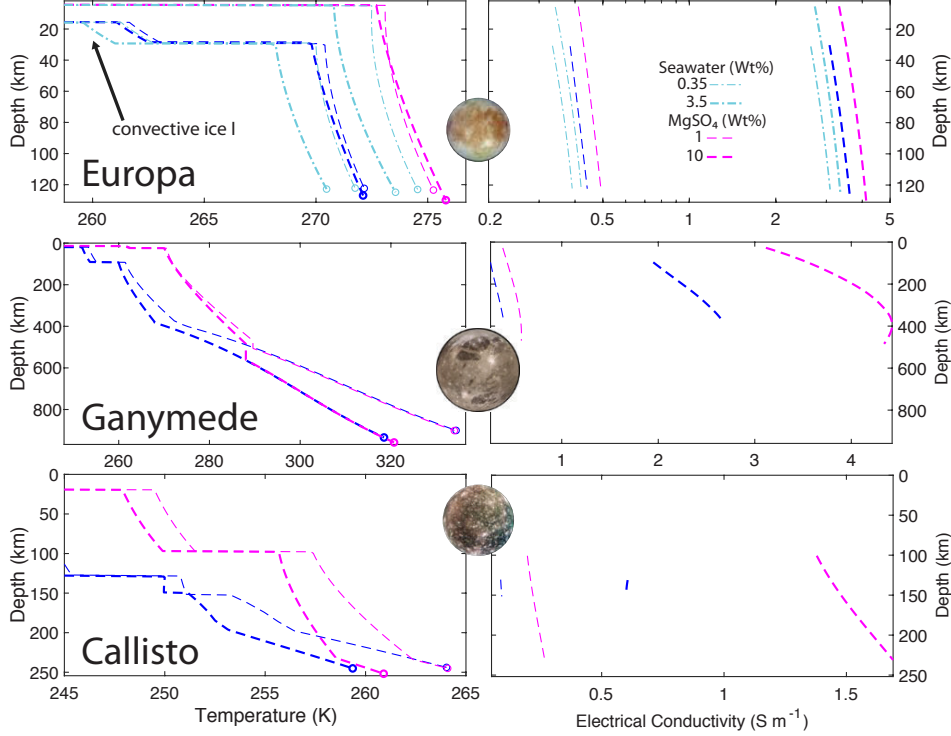


Figure 4: Adiabatic ocean temperature (left) and electrical conductivity (right). Convecting oceans with  $\text{MgSO}_4$  (dashed lines) are warmer. Standard seawater (mostly  $\text{NaCl}$ ; dot-dashed lines) creates colder oceans and lower electrical conductivities. Thicker ice (blue), corresponds to colder adiabatic profiles in the underlying oceans, which also lowers electrical conductivity. Open and closed circles correspond to the inferred depth to the upper boundary of the silicate layer for the saline and pure water oceans, respectively. Conductivities in the liquid regions are several orders of magnitude larger than in the ice and rock. Adapted from Vance et al. (2018).

under the high-pressure ice, it will create an induction response at low frequencies, as discussed below.

### 3.3 Amplitude and Phase Lag of the Diffusive Response

The normalized surface induction response for Europa, Ganymede, and Callisto, shown in Fig. 5, are based on the adiabatic ocean electrical conductivity profiles shown in Fig. 4, assuming spherical symmetry (Section 2). Warmer and thus thicker oceans (magenta curves) have larger amplitude responses, corresponding to overall higher values of the conductance. The induction signatures for the adiabatic ocean profile are nearly equal to those of oceans with uniform conductivity equal to the mean of the adiabatic model (Section 2). These signatures differ, however, from those of an ocean with uniform conductivity based on the temperature and electrical conductivity at the ice-ocean interface.

For Europa, the induction signatures for modeled oxidized (10 wt%  $\text{MgSO}_4$ ) and reduced (seawater) oceans are nearly identical in their amplitude responses. However, the two ocean models show phase separation of a few degrees at the orbital frequency of  $3.6 \times 10^{-6}$  Hz (85.23 hr period).

Local enhancements in the ocean conductivity can have a discernible induction response. For Ganymede, we simulated a second ocean layer at the water–rock interface at a depth of 900 km, under 530 km of ice VI (Vance et al., 2018), modeled as a 10-km-thick high-conductivity region (20 S/m) corresponding to a nearly saturated  $\text{MgSO}_4$  solution, consistent with (Hogenboom et al., 1995) and (Calvert et al., 1958). The influence of such a layer (dotted lines in Fig. 5) is a  $\sim 4\%$  increase in the amplitude response and a corresponding  $\sim 7\%$  decrease in the phase response around  $2.3 \times 10^{-7}$  Hz. A  $\sim 1\%$  decrease in amplitude is also seen at frequencies of  $0.93 \times 10^{-6}$  Hz and  $1.6 \times 10^{-6}$  Hz.

For Callisto, there is a small range of conditions under which oceans may be present. Salty oceans considered by Vance et al. (2018) have thicknesses of 20 and 132 km. For the thinner ocean, a 96 km layer of high-pressure ice underlies the ocean. The depicted state is likely transient, as ice III is buoyant in the modeled 10wt%  $\text{MgSO}_4$  composition, and an upward snow effect should hasten the transfer of heat from the interior. Simulating a subsequent stage with ice III above the ocean awaits improved thermodynamic data, and will be discussed in future work. The present simulations illustrate the effect of the greater skin depth for the thicker and deeper ocean in terms of a higher amplitude response at lower frequencies and phase curve also shifted in the direction of lower frequencies.

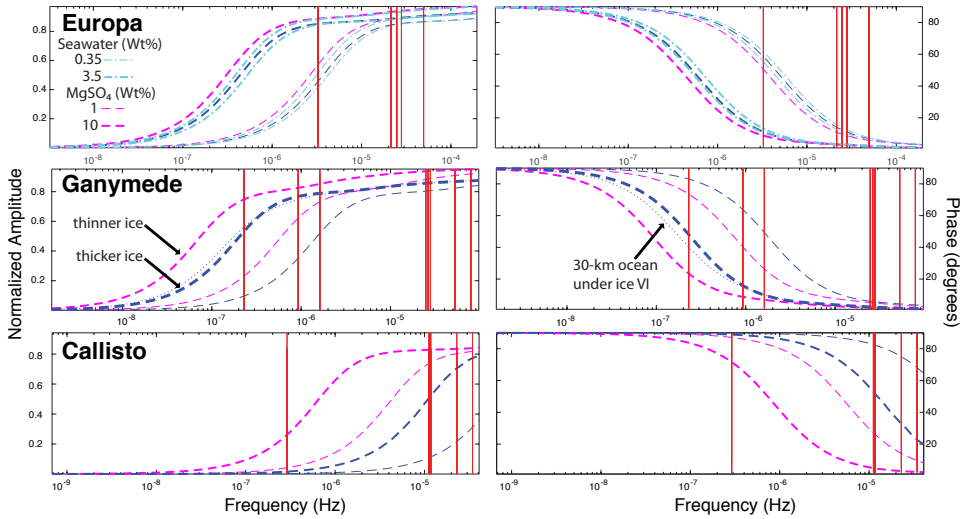


Figure 5: Normalized magnetic induction amplitudes (left) and phases (right) for the conductivity profiles in Fig. 4, at frequencies including the induction peaks noted in Fig. 1 (vertical red lines).

### 3.4 Mean Diffusive Response Relative to the Imposed Field

For the sake of comparing the passive induction responses of Europa, Ganymede and Callisto with fields induced by oceanic flows, we introduce the residual field,  $B_R$ . This quantity allows us to quickly examine the frequency dependent induction response for a given interior model, accounting for both the amplitude ( $A$ ) and phase shift ( $\phi$ ). For the geometric mean frequency components of Jupiter’s field ( $|B| = \sqrt{B_x^2 + B_y^2 + B_z^2}$ ), we define  $B_R$  as

$$B_R = |B|(\cos \phi - A) \quad (52)$$

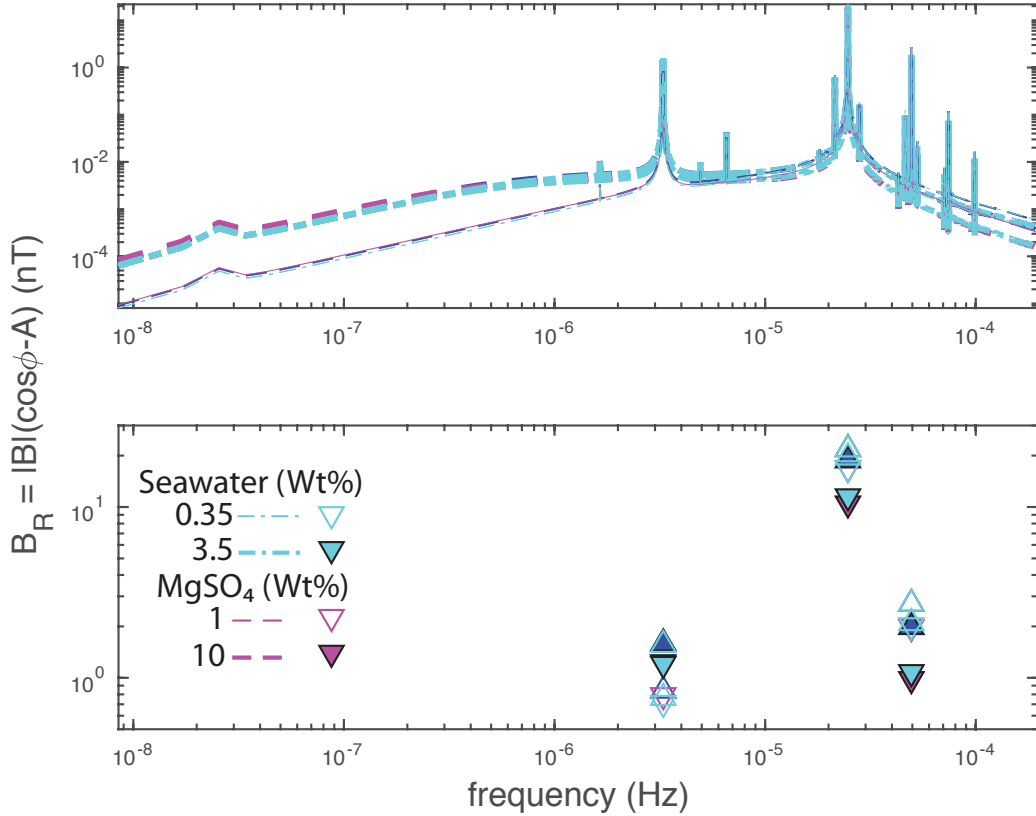


Figure 6: Europa: Residual field ( $B_R$ ) of the diffusive induction response. Thick lines are higher salinities (10wt% and 3.5wt%, respectively) for oceans with aqueous  $\text{MgSO}_4$  (magenta and blue  $---$ ) and seawater (cyan dash-dot). Thinner lines are for oceans with 10% of those concentrations. The lower pane shows responses at the strongest inducing frequencies in Figure 1. Filled symbols are for the higher concentrations. Upward triangles are for thicker ice (30 km) and downward triangles are for thinner ice (5 km).

More information can be gained by examining the directional components of Jupiter’s field (Figure 1).

Figures 6, 7, and 8 show the spectra of residual fields for Europa, Ganymede, and Callisto, respectively. Subpanels in each figure isolate the peak responses at the main driving frequencies shown in Figure 1. Tables 1, 2, and 3 include the corresponding data. Figures S1-S3 illustrate possible errors arising from analyses assuming a uniform conductivity of the ocean. They plot the deviations (in percent) between the residual fields ( $B_R$ ) of the adiabatic oceans (Figure 4) and the equivalent responses obtained by giving the oceans uniform conductivity, either as the equivalent mean value or the value at the top of the ocean (i.e. at the ice–ocean interface).

#### 4 Magnetic Induction from Oceanic Fluid Flows

Another component of the induced magnetic response might occur in the icy Galilean satellites, arising not from Jupiter’s changing magnetic field, but from charges moving with oceanic fluid flows. Such induced magnetic fields are typically neglected

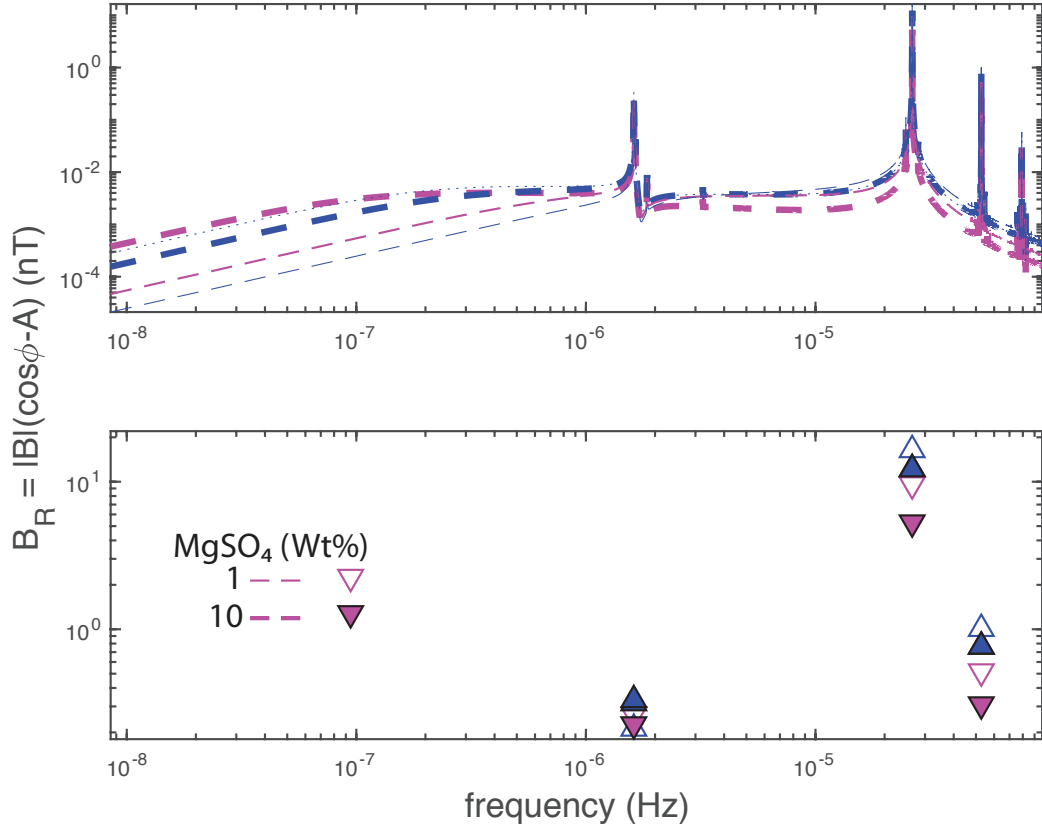


Figure 7: Ganymede: Residual field ( $B_R$ ) of the diffusive induction response. Thick lines are higher salinities (10wt%) for oceans with aqueous  $\text{MgSO}_4$  (magenta and blue  $---$ ). Thinner lines are for oceans with 1wt%  $\text{MgSO}_4$ . The dotted line is for the case with a 30-km-thick oceanic layer underneath the high-pressure ice. The lower pane shows responses at the strongest inducing frequencies in Figure 1. Filled symbols are for the higher concentrations. Upward triangles are for thicker ice ( $\sim 100$  km) and downward triangles are for thinner ice ( $\sim 30$  km)

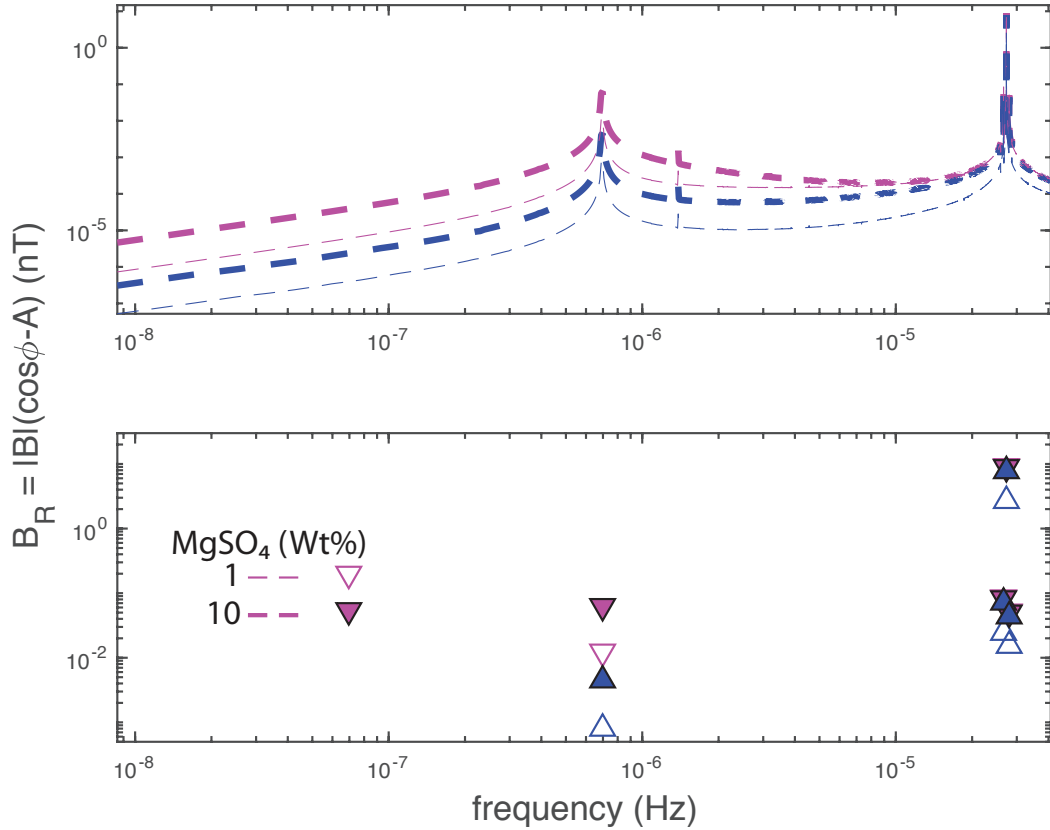


Figure 8: Callisto: Residual field ( $B_R$ ) of the diffusive induction response. Thick lines are higher salinities (10wt%) for oceans with aqueous  $\text{MgSO}_4$  (magenta and blue  $--$ ). Thinner lines are for oceans with 1wt%  $\text{MgSO}_4$ . The lower pane shows responses at the strongest inducing frequencies in Figure 1. Filled symbols are for the higher concentrations. Upward triangles are for thicker ice ( $\sim 130$  km) and downward triangles are for thinner ice ( $\sim 100$  km).



	$T_b$ (K)	$T_{mean}$ (K)	$D_I$ (km)	$D_{ocean}$ (km)	$B_R$ (nT)		
Europa			$f$ ( $\times 10^{-6}$ Hz)		<b>3.25</b>	<b>24.73</b>	<b>49.46</b>
<b>MgSO<sub>4</sub> 1Wt%</b>	270.4	271.5	31	120	0.841	21.862	2.715
$\langle \sigma \rangle = 0.4227$ S m <sup>-1</sup>	270.4	271.5	31	120	0.823	21.417	2.654
$\sigma_{top} = 0.3847$ S m <sup>-1</sup>	270.4	271.5	31	120	0.769	21.304	2.650
	273.1	274.3	6	147	0.791	16.892	1.980
$\langle \sigma \rangle = 0.4640$ S m <sup>-1</sup>	273.1	274.3	6	147	0.755	15.964	1.900
$\sigma_{top} = 0.4107$ S m <sup>-1</sup>	273.1	274.3	6	147	0.702	16.122	1.928
<b>MgSO<sub>4</sub> 10Wt%</b>	269.8	271.3	30	127	1.591	18.741	1.983
$\langle \sigma \rangle = 3.4478$ S m <sup>-1</sup>	269.8	271.3	30	127	1.539	18.234	1.961
$\sigma_{top} = 3.0763$ S m <sup>-1</sup>	269.8	271.3	30	127	1.536	18.686	2.008
	272.7	274.5	5	154	1.233	10.477	0.982
$\langle \sigma \rangle = 3.8547$ S m <sup>-1</sup>	272.7	274.5	5	154	1.167	9.800	0.935
$\sigma_{top} = 3.3197$ S m <sup>-1</sup>	272.7	274.5	5	154	1.173	10.634	1.000
<b>Seawater 0.35165 Wt%</b>	270.0	271.1	31	120	0.763	21.749	2.719
$\langle \sigma \rangle = 0.3734$ S m <sup>-1</sup>	270.0	271.1	31	120	0.746	21.112	2.645
$\sigma_{top} = 0.3339$ S m <sup>-1</sup>	270.0	271.1	31	120	0.684	21.026	2.636
	272.5	273.6	6	146	0.712	16.850	2.029
$\langle \sigma \rangle = 0.3945$ S m <sup>-1</sup>	272.5	273.6	6	146	0.678	16.046	1.926
$\sigma_{top} = 0.3415$ S m <sup>-1</sup>	272.5	273.6	6	146	0.614	15.921	1.947
<b>Seawater 3.5165 Wt%</b>	268.2	269.7	31	122	1.559	19.524	2.091
$\langle \sigma \rangle = 2.9548$ S m <sup>-1</sup>	268.2	269.7	31	122	1.523	18.989	2.052
$\sigma_{top} = 2.6476$ S m <sup>-1</sup>	268.2	269.7	31	122	1.510	19.349	2.098
	270.8	272.3	5	148	1.205	11.538	1.079
$\langle \sigma \rangle = 3.1457$ S m <sup>-1</sup>	270.8	272.3	5	148	1.138	10.805	1.024
$\sigma_{top} = 2.7346$ S m <sup>-1</sup>	270.8	272.3	5	148	1.140	11.350	1.068

Table 1: Europa: Residual fields ( $B_R$ ) at the main inducing frequencies in Fig 1. For the different ocean compositions and thicknesses of the upper ice I lithosphere ( $D_I$ ; Figure 4, the adiabatic response is given first, followed by the response for the ocean with uniform conductivity set to the mean of the adiabatic ocean ( $\langle \sigma \rangle$ ), and then for the case with uniform conductivity set to the value at the ice-ocean interface ( $\sigma_{top}$ ).

because they are expected to be relatively weak. On Earth, ocean currents induce fields on the order of 100 nT in a background field of about 40,000 nT; these fields are observable by space-based magnetometers and have been used to monitor ocean currents (Constable & Constable, 2004; Tyler et al., 2003). If there are oceanic flow-driven induction signals present in the icy Galilean satellites, and if the spatial or temporal structures of these induction signals allow them to be separated from the contributions driven by variations in Jupiter’s magnetic field, it would permit characterization of the ocean flows themselves as has been done for the Earth’s ocean (e.g., Chave, 1983; Tyler et al., 2003; Grayver et al., 2016; Minami, 2017). Conversely, if such induced signals are present but the analysis does not accommodate that fact, then the recovered electrical conductivity estimates will be biased and inaccurate.

	$T_b$ (K)	$T_{mean}$ (K)	$D_I$ (km)	$D_{ocean}$ (km)	$B_R$ (nT)		
Ganymede			$f$ ( $\times 10^{-6}$ Hz)	<b>1.62</b>	<b>26.37</b>	<b>52.74</b>	
<b>MgSO<sub>4</sub> 1Wt%</b>	270.7	279.0	25	442	0.265	9.580	0.517
$\langle \sigma \rangle = 0.5166$ S m <sup>-1</sup>	270.7	279.0	25	442	0.243	8.753	0.477
$\sigma_{top} = 0.3890$ S m <sup>-1</sup>	270.7	279.0	25	442	0.229	9.601	0.516
	261.5	266.1	93	272	0.212	16.389	1.007
$\langle \sigma \rangle = 0.3295$ S m <sup>-1</sup>	261.5	266.1	93	272	0.203	15.626	0.967
$\sigma_{top} = 0.2608$ S m <sup>-1</sup>	261.5	266.1	93	272	0.175	15.906	0.999
<b>MgSO<sub>4</sub> 10Wt%</b>	270.1	278.2	28	455	0.226	5.286	0.309
$\langle \sigma \rangle = 4.0541$ S m <sup>-1</sup>	270.1	278.2	28	455	0.209	4.991	0.290
$\sigma_{top} = 3.1056$ S m <sup>-1</sup>	270.1	278.2	28	455	0.226	5.325	0.306
	260.0	263.5	96	282	0.316	12.202	0.762
$\langle \sigma \rangle = 2.3476$ S m <sup>-1</sup>	260.0	263.5	96	282	0.304	11.919	0.750
$\sigma_{top} = 1.9483$ S m <sup>-1</sup>	260.0	263.5	96	282	0.304	12.174	0.761
30 km 20 S m <sup>-1</sup> layer	260.0	263.5	96	282	0.332	12.156	0.765

Table 2: Ganymede: Residual fields ( $B_R$ ) at the main inducing frequencies in Fig 1. For the different ocean compositions and thicknesses of the upper ice I lithosphere ( $D_I$ ; Figure 4, the adiabatic response is given first, followed by the response for the ocean with uniform conductivity set to the mean of the adiabatic ocean ( $\langle \sigma \rangle$ ), and then for the case with uniform conductivity set to the value at the ice-ocean interface ( $\sigma_{top}$ ).

While Tyler (2011) discusses the possibility of magnetic remote sensing to detect resonant ocean tides on Europa in the limits of shallow water equations and thin-shell electrodynamics, we are not aware of any studies that have examined magnetic induction signatures due to other flows or for other satellites (e.g., Lemasquier et al., 2017; Gissinger & Pettdemange, 2019; Rovira-Navarro et al., 2019; Soderlund, 2019). Here, we focus on global fluid motions that may be driven by convection within the oceans of Europa, Ganymede, and Callisto, followed by estimates of the induction response that may be expected from these flows.

#### 4.1 Oceanic Fluid Motions

The majority of ocean circulation studies have focused on hydrothermal plumes at Europa, with global models being developed relatively recently (Vance & Goodman, 2009b; Soderlund et al.2014; Soderlund, 2019). Thermal convection in Europa’s ocean is expected in order to efficiently transport heat from the deeper interior that arises primarily from radiogenic and tidal heating in the mantle. Moreover, by estimating the extent to which rotation will organize the convective flows, Europa’s ocean was predicted to have quasi-three-dimensional turbulence (Soderlund et al.2014; Soderlund, 2019). As shown in Figure 9, this turbulence generates three-jet zonal flows with retrograde (westward) flow at low latitudes, prograde (eastward) flow at high latitudes, and meridional overturning circulation. Upwelling at the equator and downwelling at middle to high latitudes from this circulation effectively forms a Hadley-like cell in each hemisphere.

	$T_b$ (K)	$T_{mean}$ (K)	$D_I$ (km)	$D_{ocean}$ (km)	$B_R$ (nT)			
Callisto			$f$ ( $\times 10^{-6}$ Hz)	<b>0.69</b>	<b>26.60</b>	<b>27.29</b>	<b>27.99</b>	
<b>MgSO<sub>4</sub> 1Wt%</b>	257.4	259.6	99	132	0.012	0.085	9.201	0.052
$\langle \sigma \rangle = 0.2307 \text{ S m}^{-1}$	257.4	259.6	99	132	0.012	0.084	8.990	0.050
$\sigma_{top} = 0.1965 \text{ S m}^{-1}$	257.4	259.6	99	132	0.010	0.083	8.926	0.050
	250.8	250.9	128	21	0.001	0.024	2.688	0.015
$\langle \sigma \rangle = 0.0895 \text{ S m}^{-1}$	250.8	250.9	128	21	0.001	0.025	2.740	0.016
$\sigma_{top} = 0.0874 \text{ S m}^{-1}$	250.8	250.9	128	21	0.001	0.024	2.689	0.015
<b>MgSO<sub>4</sub> 10Wt%</b>	255.7	256.9	99	130	0.063	0.083	8.875	0.050
$\langle \sigma \rangle = 1.5256 \text{ S m}^{-1}$	255.7	256.9	99	130	0.062	0.082	8.763	0.049
$\sigma_{top} = 1.3789 \text{ S m}^{-1}$	255.7	256.9	99	130	0.058	0.082	8.822	0.049
	250.0	251.5	129	18	0.004	0.072	7.778	0.044
$\langle \sigma \rangle = 0.6025 \text{ S m}^{-1}$	250.0	251.5	129	18	0.005	0.072	7.781	0.044
$\sigma_{top} = 0.6062 \text{ S m}^{-1}$	250.0	251.5	129	18	0.005	0.072	7.790	0.044

Table 3: Callisto: Residual fields ( $B_R$ ) at the main inducing frequencies in Fig 1. For the different ocean compositions and thicknesses of the upper ice I lithosphere ( $D_I$ ; Figure 4, the adiabatic response is given first, followed by the response for the ocean with uniform conductivity set to the mean of the adiabatic ocean ( $\langle \sigma \rangle$ ), and then for the case with uniform conductivity set to the value at the ice-ocean interface ( $\sigma_{top}$ ).

Application of these calculations to Ganymede suggests convection is expected within its ocean as well and may have similar convective flows, although there is significantly more uncertainty in the predicted convective regime (Soderlund, 2019). Convection in Callisto’s potential ocean may be in the double-diffusive regime if the ocean’s composition is nearly saturated (Vance et al., 2018). However, considering thermal convection as an upper bound, application of the scaling arguments in Soderlund (2019) to Callisto suggest similar ocean flows may be expected here as well.

The nominal ocean model shown in Figure 9 is, therefore, applicable to all three ocean worlds considered here. As described in Soderlund (2019), the model was carried out using the MagIC code (Wicht, 2002) with the SHTns library for the spherical harmonics transforms (Schaeffer, 2013) and is characterized by the following dimensionless input parameters: shell geometry  $\chi = r_i/r_o = 0.9$ , Prandtl number  $Pr = \nu/\kappa = 1$ , Ekman number  $E = \nu/\Omega D^2 = 3.0 \times 10^{-4}$ , and Rayleigh number  $Ra = \alpha g \Delta T D^3/\nu\kappa$ , where  $r_i$  and  $r_o$  are the inner and outer radii of the ocean,  $D = r_o - r_i$  is ocean thickness,  $\Omega$  is rotation rate,  $\nu$  is kinematic viscosity,  $\kappa$  is thermal diffusivity,  $\alpha$  is thermal expansivity,  $g$  is gravitational acceleration, and  $\Delta T$  is superadiabatic temperature contrast. The boundaries are impenetrable, stress-free, and isothermal.

The model outputs, such as the velocity field, are also non-dimensional. For example, the Rossby number  $Ro = U/\Omega D$  is the ratio of rotational  $\Omega^{-1}$  to inertial  $D/U$  timescales that allows the dimensional flow speeds to be determined:  $U = \Omega D Ro$  using ocean thickness  $D$  as the length scale and rotation rates  $\Omega = [2.1 \times 10^{-5}, 1.0 \times 10^{-5}, 4.4 \times 10^{-6}] \text{ s}^{-1}$  for Europa, Ganymede, and Callisto, respectively. Following Table 1, European ocean thicknesses of 120–154 km are considered. This range of liquid ocean thicknesses extends to 272 – 455 km for Ganymede (Table 2) and 18 – 132 km for Callisto (Table 3), given the larger uncertainties on their internal structures. We

therefore assume the following mean parameter values in Figure 9:  $D_{Europa} = 135$  km,  $D_{Ganymede} = 360$  km, and  $D_{Callisto} = 75$  km, with the ranges considered in Table 4. Flows are fastest for Ganymede and Europa, where the zonal jets can reach m/s speeds, the mean latitudinal flows have peak speeds of tens of cm/s, and the mean radial flows are  $\sim 10$  cm/s.

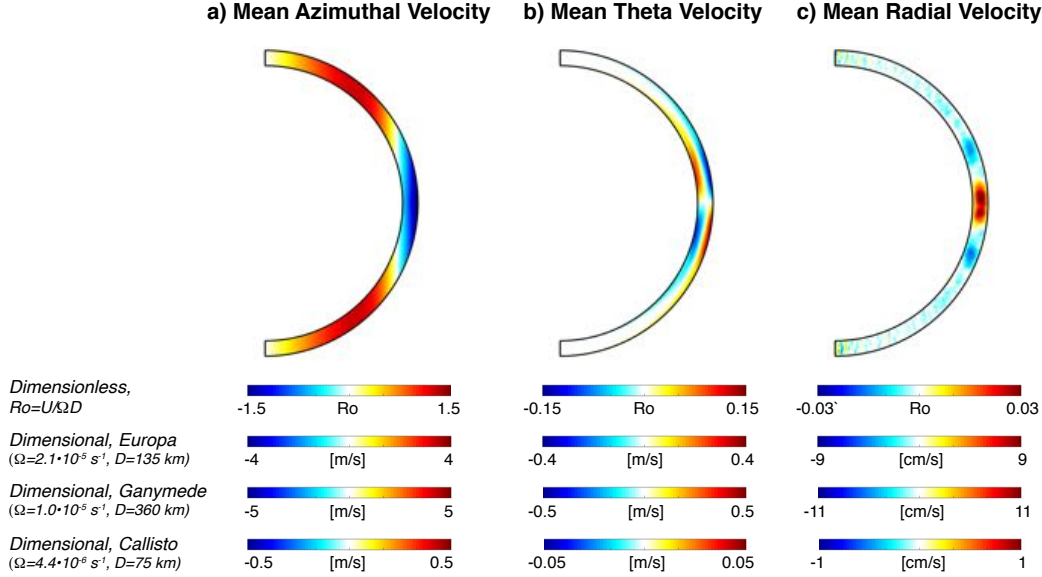


Figure 9: Mean flow fields in our nominal global ocean model from Soderlund (2019), averaged over 18 planetary rotations and all longitudes. **a)** Zonal velocity field where red denotes prograde flows and blue denotes retrograde flows. **b)** Theta velocity field where red denotes away from the north pole and blue denotes toward the north pole. **c)** Radial velocity field where red denotes upwelling flows and blue denotes downwelling flows.

## 4.2 Generation of Induced Magnetic Fields

The magnetic induction equation can be used to estimate the components of the magnetic field  $\mathbf{B}$  induced by ocean currents with velocity  $\mathbf{u}$  and those arising from changes in the externally imposed field:

$$\frac{\partial \mathbf{B}}{\partial t} = \nabla \times (\mathbf{u} \times \mathbf{B}) - \nabla \times (\eta \nabla \times \mathbf{B}) \quad (53)$$

where  $\eta = (\mu_0 \sigma)^{-1}$  is the magnetic diffusivity. Here, the first term represents the evolution of the magnetic field, the second term represents magnetic induction, and the third term represents magnetic diffusion.

Neglecting variations in oceanic electrical conductivity with depth and assuming an incompressible fluid, equation 53 simplifies to

$$\frac{\partial \mathbf{B}}{\partial t} = (\mathbf{B} \cdot \nabla) \mathbf{u} - (\mathbf{u} \cdot \nabla) \mathbf{B} + \eta \nabla^2 \mathbf{B}, \quad (54)$$

after also expanding the induction term and utilizing  $\nabla \cdot \mathbf{B} = 0$  and  $\nabla \cdot \mathbf{u} = 0$ . Let us decompose the total magnetic field into jovian imposed  $\mathbf{F}$  and the satellite's induced  $\mathbf{b}$  field components:

$$\mathbf{B} = \mathbf{F} + \mathbf{b} \quad (55)$$

with  $|\mathbf{F}| \gg |\mathbf{b}|$ . The induction equation then becomes

$$\frac{\partial \mathbf{b}}{\partial t} = -\frac{\partial \mathbf{F}}{\partial t} + (\mathbf{F} \cdot \nabla) \mathbf{u} - (\mathbf{u} \cdot \nabla)(\mathbf{F} + \mathbf{b}) + \eta \nabla^2 (\mathbf{F} + \mathbf{b}) \quad (56)$$

Here, the first term is the evolution of the induced magnetic field, the second term is induction due to variations in Jupiter's magnetic field, the third term is induction due to oceanic fluid motions, the fourth term is advection of the field by ocean flows, and the fifth and sixth terms are diffusion of the Jovian and induced fields.

Let us next assume that the Jovian field can be approximated by  $\mathbf{F} = F_o \hat{\mathbf{z}}$ , where  $F_o$  is constant and homogeneous and  $\hat{\mathbf{z}}$  is aligned with the rotation axis, in which case equation 56 further simplifies to:

$$\frac{\partial \mathbf{b}}{\partial t} = F_o \frac{\partial \mathbf{u}}{\partial z} - (\mathbf{u} \cdot \nabla) \mathbf{b} + \eta \nabla^2 \mathbf{b}. \quad (57)$$

We will also focus on the quasi-steady induction signal generated by ocean flows rather than the rapidly varying contribution that could be difficult to distinguish from other magnetic field perturbations. Towards this end, the induced magnetic field and velocity fields are decomposed into mean and fluctuating components:  $\mathbf{b} = \bar{\mathbf{b}} + \mathbf{b}'$  and  $\mathbf{u} = \bar{\mathbf{u}} + \mathbf{u}'$ . Inserting this into equation 57 and using Reynolds averaging yields

$$\frac{\partial \bar{\mathbf{b}}}{\partial t} = F_o \frac{\partial \bar{\mathbf{u}}}{\partial z} - (\bar{\mathbf{u}} \cdot \nabla) \bar{\mathbf{b}} - \overline{(\mathbf{u}' \cdot \nabla) \mathbf{b}'} + \eta \nabla^2 \bar{\mathbf{b}}. \quad (58)$$

Next, we focus on the radial and latitudinal components because the zonal flow ( $\bar{u}_\phi$ ) is nearly invariant in the z-direction (Figure 9a), noting also that azimuthally oriented (toroidal) magnetic fields would not be detectable by spacecraft:

$$\frac{\partial \bar{b}_r}{\partial t} = F_o \frac{\partial \bar{u}_r}{\partial z} - (\bar{\mathbf{u}} \cdot \nabla) \bar{b}_r - \overline{(\mathbf{u}' \cdot \nabla) b'_r} + \eta \nabla^2 \bar{b}_r \quad (59)$$

$$\frac{\partial \bar{b}_\theta}{\partial t} = F_o \frac{\partial \bar{u}_\theta}{\partial z} - (\bar{\mathbf{u}} \cdot \nabla) \bar{b}_\theta - \overline{(\mathbf{u}' \cdot \nabla) b'_\theta} + \eta \nabla^2 \bar{b}_\theta \quad (60)$$

Using simple scaling arguments, the second and third terms on the right sides are likely small compared to the first term since  $|F| \gg |b|$  (assuming similar characteristic flow speeds and length scales) such that

$$\frac{\partial \bar{b}_r}{\partial t} \approx F_o \frac{\partial \bar{u}_r}{\partial z} + \eta \nabla^2 \bar{b}_r \quad (61)$$

$$\frac{\partial \bar{b}_\theta}{\partial t} \approx F_o \frac{\partial \bar{u}_\theta}{\partial z} + \eta \nabla^2 \bar{b}_\theta. \quad (62)$$

In the steady state limit and approximating the gradient length scales as  $D$  and flow speeds as  $U_r$  and  $U_\theta$ , the magnetic fields induced by ocean currents can be estimated as:

$$\frac{F_o U_r}{D} \sim \frac{\eta b_r}{D^2} \text{ such that } b_r \sim \frac{F_o U_r D}{\eta} = \mu_o \sigma D U_r F_o \quad (63)$$

$$\frac{F_o U_\theta}{D} \sim \frac{\eta b_\theta}{D^2} \text{ such that } b_\theta \sim \frac{F_o U_\theta D}{\eta} = \mu_o \sigma D U_\theta F_o. \quad (64)$$

The resulting induced magnetic fields are then stronger for larger electrical conductivities, ocean thicknesses, flow velocities, and satellites closer to the host planet, since  $F_o$  decreases with distance.

Table 4 summarizes the ambient Jovian conditions at Europa, Ganymede, and Callisto as well as the relevant characteristics of their oceans, and the computed upper bounds on the induced magnetic field strengths. Here, we assume flow speeds typical

of the global, steady overturning cells due to their temporal persistence and large spatial scale, which we hypothesize will produce the strongest induced magnetic signature that would be detectable at spacecraft altitudes. We find that the theta magnetic field components are larger than the radial components by roughly a factor of five, reaching  $\sim 200$  nT for both Europa and Ganymede (higher salt content, thinner ice shell models); estimates can be an order of magnitude weaker in the lower salt content, thicker ice shell models). The radial variations correspond to signals up to 33% (Ganymede) and 8% (Europa) of the ambient Jovian field, which could be detectable with future missions. The signature at Callisto is small ( $\lesssim 1$  nT). In addition, we predict the fields to be strongest near the equator where large vertical gradients in the convective flows exist (Figure 9b-c).

	$\sigma$ [S/m]	$D$ [km]	$U_r$ [m/s]	$U_\theta$ [m/s]	$F_o$ [nT]	$b_r$ [nT]	$b_\theta$ [nT]
<b>Europa</b>							
MgSO <sub>4</sub> 1 Wt%, Thicker ice shell	0.4	120	0.08	0.38	420	2	10
MgSO <sub>4</sub> 1 Wt%, Thinner ice shell	0.5	147	0.09	0.46	420	3	18
MgSO <sub>4</sub> 10 Wt%, Thicker ice shell	3.4	127	0.08	0.40	420	18	91
MgSO <sub>4</sub> 10 Wt%, Thinner ice shell	3.9	154	0.10	0.49	420	32	155
Seawater 0.35 Wt%, Thicker ice shell	0.4	120	0.08	0.38	420	2	10
Seawater 0.35 Wt%, Thinner ice shell	0.4	146	0.09	0.46	420	3	14
Seawater 3.5 Wt%, Thicker ice shell	3.0	122	0.08	0.38	420	15	73
Seawater 3.5 Wt%, Thinner ice shell	3.1	148	0.09	0.47	420	22	114
<b>Ganymede</b>							
MgSO <sub>4</sub> 1 Wt%, Thicker ice shell	0.3	272	0.08	0.41	120	1	5
MgSO <sub>4</sub> 1 Wt%, Thinner ice shell	0.5	442	0.13	0.66	120	4	22
MgSO <sub>4</sub> 10 Wt%, Thicker ice shell	2.3	282	0.08	0.42	120	8	41
MgSO <sub>4</sub> 10 Wt%, Thinner ice shell	4.1	455	0.14	0.68	120	39	191
<b>Callisto</b>							
MgSO <sub>4</sub> 1 Wt%, Thicker ice shell	0.09	21	0.003	0.01	35	$\ll 1$	$\ll 1$
MgSO <sub>4</sub> 1 Wt%, Thinner ice shell	0.2	132	0.02	0.09	35	0.02	0.1
MgSO <sub>4</sub> 10 Wt%, Thicker ice shell	0.6	18	0.002	0.01	35	$\ll 1$	$\ll 1$
MgSO <sub>4</sub> 10 Wt%, Thinner ice shell	1.5	130	0.02	0.09	35	0.2	0.8

Table 4: Assumed properties and resulting calculated upper bounds on the strengths of the magnetic fields induced by oceanic fluid flows. Ambient magnetic field strengths,  $F_o$ , from Showman & Malhotra (1999); radial and theta flow speeds,  $U_r$  and  $U_\theta$  with  $U = \Omega DRo$ , from Figure 9; ocean thicknesses,  $D$ , from Vance et al. (2018); and electrical conductivity,  $\sigma$ , from Figure 4. These signals are anticipated to be largest near the equator where  $U_\theta$  and  $U_r$  are strongest, as indicated in Figure 9b-c.

The simplified approach shown above gives an order of magnitude estimate of the maximum induced field. Future work will assess the implications of these assumptions through more detailed calculations. For example, we have assumed a homogeneous and constant Jovian field; however, the magnetic environment throughout the orbit close in to Jupiter may be highly variable and the external field is affected by the presence of heavy ions and a variable magnetosphere dynamics throughout a single orbit (e.g., Schilling et al., 2008). The temporal and spatial variation of the ambient field is expected to be significant and the influence of these variations on ocean flow-driven

magnetic field signatures remains to be explored. Kinematic models that directly solve the coupled momentum and induction equations are also an exciting avenue to refine these estimates.

## 5 Discussion and Conclusions

The inverse problem of reconstructing the full induction response is complex and is discussed in detail elsewhere (e.g., Khurana et al., 2009, and Cochrane et al. *in progress*). Here, we focus instead on how the adiabatic conductivity profile of the ocean affects the induction response relative to the mean case that is usually considered in space physics analyses (e.g., Kivelson et al., 2000), and relative to the isothermal case often considered in analyses of interior structure (e.g., Schubert et al., 2004).

Differences between the adiabatic and mean conductivity cases have less dependence on frequency (Tables 1-3 and Figures S1, S3, and S5). For Europa, the nominal oceans with ice shells 5- and 30-km thick have errors of about 6% and 3%, respectively, and amount to nearly a 1 nT difference for the largest signals that exceed 20 nT. For Ganymede, the nominal oceans with ice shells  $\sim$ 25- and  $\sim$ 100-km thick have errors of about 7% and 3%, and are also nearly 1 nT for the largest signals that exceed 10 nT. For Callisto, the induction response of the mean conductivity ocean for ice shells of  $\sim$ 100- and  $\sim$ 130-km thickness is within about 2% of the response for the adiabatic ocean, less than 0.3 nT for the largest signals that approach 10 nT.

The induction response of the adiabatic ocean differs from that of the equivalent ocean with the conductivity of fluid at the ice-ocean interface. The greater mismatch of conductivities of the lower part of the ocean causes large differences in amplitude and phase at lower frequencies (i.e. for larger skin depths). For Europa, this means that the lower-frequency mean-motion signal ( $3.2 \times 10^{-6}$  Hz; Table 1) differs by more than 15% for the warmer lower-salinity oceans, or about 0.1 nT. For Ganymede, the differences at the mean-motion frequency ( $1.62 \times 10^{-6}$  Hz; Table 2) can approach 25%, which amounts to 0.04 nT. For Callisto, the differences at the mean-motion frequency ( $6.9 \times 10^{-7}$  Hz; Table 3) approach 20%, which amounts to only 2 pT for the small predicted residual field based on the mean field. By contrast, the higher-frequency diurnal signals differ by less than 5%.

Based on the circulation models and upper bound induced magnetic field estimates described in Section 4, flow-induced fields may be a prominent component of the magnetic fields measured in the low latitudes for Europa and Ganymede. The peak flow-induced magnitude is 30-40 nT (Table 4) compared with Jovian-induced residual fields of less than 20 nT for both Europa (Table 1) and Ganymede (Table 2).

### 5.1 Implications for future missions

The Europa Clipper mission will conduct multiple ( $>40$ ) flybys of Europa, and will investigate its induction response with the goal of constraining the ocean conductivity to within  $\pm 0.5$  S  $\text{m}^{-1}$  and ice thickness to within  $\pm 2$  km (Buffington et al., 2017). The flybys at high latitudes will allow the Europa Clipper investigation to isolate flow-induced fields from the diffusive response, and possibly to derive constraints on currents in the ocean. With independent constraints on ice thickness obtained from the Radar for Europa Assessment and Sounding: Ocean to Near-surface (REASON) and Europa Imaging System (EIS) investigations (Steinbrügge et al., 2018), it may be possible to constrain the ocean's temperature and thus the adiabatic structure for the best-fit ocean composition inferred from compositional investigations. The analyses provided here (Figure 6 and Table 1) indicate that a sensitivity of 1.5 nT is probably insufficient to distinguish between end-member  $\text{MgSO}_4$  and NaCl oceans, but might be sufficient to distinguish between order-of-magnitude differences in salinity.

The Jupiter ICy moons Explorer (JUICE) will execute two Europa flybys and nine Callisto flybys, and will orbit Ganymede (Grasset et al., 2013). The magnetic field investigation seeks to determine the induction response to better than 0.1 nT. The Europa flybys might aid the Europa Clipper investigation in constraining the composition of the ocean. At Ganymede, the magnetic field investigation will not be sufficient to discern the presence of a basal liquid layer at the ice VI-rock interface. Although the ability to discern between ocean compositions could not be assessed owing to insufficient electrical conductivity data at high pressures, it seems likely that useful constraints could be derived based on the signal strengths at Ganymede, if laboratory-derived electrical conductivity data for relevant solutions under pressure became available. At Callisto, 0.1 nT accuracy may only allow sensing of the induction response to Jupiter’s synodic field, which might be sufficient to infer the thickness and salinity of an ocean if adequate temporal coverage is obtained to confirm the phase of the response.

### Acknowledgments

Work by JPL co-authors was partially supported by the Jet Propulsion Laboratory, Caltech, and by the Icy Worlds node of NASA’s Astrobiology Institute (13-13NAI7\_2-0024). This work was partially supported by NASA’s Europa Clipper project. Work by MJS was supported by the NASA Earth and Space Science Fellowship Program - Grant 80NSSC18K1236. Work by KMS was also supported by NASA Grant NNX14AR28G.

The Matlab scripts and associated data needed to compute the results shown here are currently being archived. The data and scripts for radial structure models and diffusive induction will be placed on github (<https://github.com/vancesteven/PlanetProfile>) and Zenodo.

The MagIC code is publicly available at the <https://magic-sph.github.io/contents.html> website. All global convection model data were first published in Soderlund et al. (2019) and are available therein.

©2020. All rights reserved.

### References

- Acuna, M. H., & Ness, N. F. (1976, Jun). The main magnetic field of jupiter. *Journal of Geophysical Research*, 81(16), 2917–2922. Retrieved from <http://dx.doi.org/10.1029/JA081i016p02917> doi: 10.1029/ja081i016p02917
- Buffington, B., Lam, T., Campagnola, S., Ludwinski, J., Ferguson, E., Bradley, B., ... Siddique, F. (2017). Evolution of trajectory design requirements on NASA’s planned Europa Clipper mission. *Proceedings of the 68th International Astronautical Congress (IAC)(IAC-17-C1.7.8)*.
- Calvert, R., Cornelius, J. A., Griffiths, V. S., & Stock, D. I. (1958). The determination of the electrical conductivities of some concentrated electrolyte solutions using a transformer bridge. *The Journal of Physical Chemistry*, 62(1), 47–53.
- Chave, A. D. (1983). On the theory of electromagnetic induction in the Earth by ocean currents. *J. Geophys. Res.*, 88, 3531–3542.
- Choblet, G., Tobie, G., Sotin, C., Kalousová, K., & Grasset, O. (2017, Mar). Heat transport in the high-pressure ice mantle of large icy moons. *Icarus*, 285, 252–262. Retrieved from <http://dx.doi.org/10.1016/j.icarus.2016.12.002> doi: 10.1016/j.icarus.2016.12.002
- Connerney, J., Acuna, M., Ness, N., & Satoh, T. (1998). New models of Jupiter’s magnetic field constrained by the Io flux tube footprint. *Journal of Geophysical Research: Space Physics*, 103(A6), 11929–11939.
- Connerney, J. E. P., Kotsiaros, S., Oliverson, R. J., Espley, J. R., Joergensen, J. L.,



- Joergensen, P. S., ... et al. (2018, Mar). A new model of Jupiter's magnetic field from Juno's first nine orbits. *Geophysical Research Letters*, *45*(6), 2590–2596. Retrieved from <http://dx.doi.org/10.1002/2018GL077312> doi: 10.1002/2018gl077312
- Constable, S., & Constable, C. G. (2004). Observing geomagnetic induction in magnetic satellite measurements and associated implications for mantle conductivity. *Geochem. Geophys. Geosys.*, *5*, Q01006.
- Gissinger, C., & Petitdemange, L. (2019). A magnetically driven equatorial jet in Europa's ocean. *Nature Astron.*, *1*.
- Grasset, O., Dougherty, M., Coustenis, A., Bunce, E., Erd, C., Titov, D., ... others (2013). Jupiter icy moons explorer (juice): An esa mission to orbit ganymede and to characterise the jupiter system. *Planetary and Space Science*, *78*, 1–21.
- Grayver, A. V., Schnepf, N. R., Kuvshinov, A. V., Sabaka, T. J., Manoj, C., & Olsen, N. (2016). Satellite tidal magnetic signals constrain oceanic lithosphere-aesthenosphere boundary. *Science Adv.*, *2*(9), e1600798.
- Hand, K., & Chyba, C. (2007). Empirical constraints on the salinity of the european ocean and implications for a thin ice shell. *Icarus*, *189*(2), 424–438.
- Hartkorn, O., & Saur, J. (2017, Nov). Induction signals from Callisto's ionosphere and their implications on a possible subsurface ocean. *Journal of Geophysical Research: Space Physics*, *122*(11), 11,677–11,697. Retrieved from <http://dx.doi.org/10.1002/2017JA024269> doi: 10.1002/2017ja024269
- Hogenboom, D. L., Kargel, J. S., Ganasan, J. P., & Lee, L. (1995, June). Magnesium sulfate-water to 400 MPa using a novel piezometer: Densities, phase equilibria, and planetological implications. *Icarus*, *115*(2), 258–277. Retrieved from <http://www.sciencedirect.com/Science/article/B6WGF-45NJJ40-14/2/5f176b700065df4efb2e1eba3abd3224>
- Journaux, B., Daniel, I., Caracas, R., Montagnac, G., & Cardon, H. (2013, Sep). Influence of NaCl on ice VI and ice VII melting curves up to 6GPa, implications for large icy moons. *Icarus*, *226*(1), 355–363. Retrieved from <http://dx.doi.org/10.1016/j.icarus.2013.05.039> doi: 10.1016/j.icarus.2013.05.039
- Journaux, B., Daniel, I., Petitgirard, S., Cardon, H., Perrillat, J.-P., Caracas, R., & Mezouar, M. (2017, Apr). Salt partitioning between water and high-pressure ices. implication for the dynamics and habitability of icy moons and water-rich planetary bodies. *Earth and Planetary Science Letters*, *463*, 36–47. Retrieved from <http://dx.doi.org/10.1016/j.epsl.2017.01.017> doi: 10.1016/j.epsl.2017.01.017
- Khurana, K., Kivelson, M., Hand, K., & Russell, C. (2009). Electromagnetic induction from Europa's ocean and the deep interior. *Europa, Edited by Robert T. Pappalardo, William B. McKinnon, Krishan K. Khurana; with the assistance of René Dotson with 85 collaborating authors. University of Arizona Press, Tucson, 2009. The University of Arizona space science series ISBN: 9780816528448, p. 571, 1, 571.*
- Khurana, K., Kivelson, M., Stevenson, D., Schubert, G., Russell, C., Walker, R., & Polansky, C. (1998). Induced magnetic fields as evidence for subsurface oceans in Europa and Callisto. *Nature*, *395*(6704), 777–780.
- Khurana, K. K. (1997, Jun). Euler potential models of Jupiter's magnetospheric field. *Journal of Geophysical Research: Space Physics*, *102*(A6), 11295–11306. Retrieved from <http://dx.doi.org/10.1029/97JA00563> doi: 10.1029/97ja00563
- Kivelson, M., Khurana, K., Russell, C., Volwerk, M., Walker, R., & Zimmer, C. (2000). Galileo magnetometer measurements: A stronger case for a subsurface ocean at Europa. *Science*, *289*, 1340–1343.
- Lainey, V., Duriez, L., & Vienne, A. (2006). Synthetic representation of the Galilean satellites' orbital motions from L1 ephemerides. *A&A*, *456*, 783–788.
- Lemasquerier, D., Grannan, A. M., Vidal, J., Cébron, D., Favier, B., Le Bars, M., &

- Aurnou, J. M. (2017). Libration-driven flows in ellipsoidal shells. *J. Geophys. Res. Planets*, *122*(9), 1926–1950.
- Lieske, J. (1998). Galilean satellite ephemerides E5. *Astronomy and Astrophysics Supplement Series*, *129*(2), 205–217.
- Liuzzo, L., Feyerabend, M., Simon, S., & Motschmann, U. (2015, Nov). The impact of Callisto’s atmosphere on its plasma interaction with the jovian magnetosphere. *Journal of Geophysical Research: Space Physics*, *120*(11), 9401–9427. Retrieved from <http://dx.doi.org/10.1002/2015JA021792> doi: 10.1002/2015ja021792
- McDougall, T. J., & Barker, P. M. (2011). Getting started with TEOS-10 and the Gibbs Seawater (GSW) oceanographic toolbox. *SCOR/IAPSO WG*, *127*, 1–28.
- Minami, T. (2017). Motional induction by tsunamis and ocean tides: 10 years of progress. *Surv. Geophys.*, *38*, 1097–1132.
- Pasek, M. A., & Greenberg, R. (2012). Acidification of Europa’s subsurface ocean as a consequence of oxidant delivery. *Astrobiology*, *12*(2), 151–159.
- Rovira-Navarro, M., Rieutord, M., Gerkema, T., Maas, L. R., van der Wal, W., & Vermeersen, B. (2019). Do tidally-generated inertial waves heat the subsurface oceans of Europa and Enceladus? *Icarus*, *321*, 126–140.
- Saur, J., Neubauer, F. M., & Glassmeier, K.-H. (2009, Dec). Induced magnetic fields in solar system bodies. *Space Science Reviews*, *152*(1-4), 391–421. Retrieved from <http://dx.doi.org/10.1007/s11214-009-9581-y> doi: 10.1007/s11214-009-9581-y
- Saur, J., Strobel, D. F., & Neubauer, F. M. (1998, Aug). Interaction of the jovian magnetosphere with Europa: Constraints on the neutral atmosphere. *Journal of Geophysical Research: Planets*, *103*(E9), 19947–19962. Retrieved from <http://dx.doi.org/10.1029/97JE03556> doi: 10.1029/97je03556
- Schaeffer, N. (2013). Efficient spherical harmonic transforms aimed at pseudospectral numerical simulations. *Geochem. Geophys. Geosy.*, *14*(3), 751–758.
- Schilling, N., Neubauer, F., & Saur, J. (2008). Influence of the internally induced magnetic field on the plasma interaction of Europa. *Journal of Geophysical Research: Space Physics*, *113*(A3).
- Schilling, N., Neubauer, F. M., & Saur, J. (2007). Time-varying interaction of Europa with the jovian magnetosphere: Constraints on the conductivity of Europa’s subsurface ocean. *Icarus*, *192*(1), 41–55.
- Schmidt, C., & Manning, C. (2017). Pressure-induced ion pairing in MgSO<sub>4</sub> solutions: Implications for the oceans of icy worlds. *Geochemical Perspectives Letters*, *3*, 66–74.
- Schubert, G., Anderson, J., Spohn, T., & McKinnon, W. (2004). Interior composition, structure and dynamics of the Galilean satellites. *Jupiter: The Planet, Satellites and Magnetosphere*, 281–306.
- Seidelmann, P., & Divine, N. (1977). Evaluation of Jupiter longitudes in system iii (1965). *Geophysical Research Letters*, *4*(2), 65–68.
- Seufert, M., Saur, J., & Neubauer, F. M. (2011). Multi-frequency electromagnetic sounding of the Galilean moons. *Icarus*, *214*(2), 477–494.
- Showman, A. P., & Malhotra, R. (1999). The Galilean satellites. *Science*, *286*(5437), 77–84.
- Soderlund, K., Schmidt, B., Wicht, J., & Blankenship, D. (2014). Ocean-driven heating of Europa’s icy shell at low latitudes. *Nature Geoscience*, *7*(1), 16–19.
- Soderlund, K. M. (2019). Ocean dynamics of outer solar system satellites. *Geophys. Res. Lett.*, <https://doi.org/10.1029/2018GL081880>.
- Steinbrügge, G., Schroeder, D., Haynes, M., Hussmann, H., Grima, C., & Blankenship, D. (2018, Jan). Assessing the potential for measuring Europa’s tidal Love number h<sub>2</sub> using radar sounder and topographic imager data. *Earth and Planetary Science Letters*, *482*, 334–341. Retrieved from <http://dx.doi.org/10.1016/j.epsl.2017.11.028> doi: 10.1016/j.epsl.2017.11.028

- Tyler, R. H. (2011). Magnetic remote sensing of Europa's ocean tides. *Icarus*, *211*, 906–908.
- Tyler, R. H., Boyer, T. P., Minami, T., Zweng, M. M., & Reagan, J. R. (2017, Nov). Electrical conductivity of the global ocean. *Earth, Planets and Space*, *69*(1). Retrieved from <http://dx.doi.org/10.1186/s40623-017-0739-7> doi: 10.1186/s40623-017-0739-7
- Tyler, R. H., Maus, S., & Luhr, H. (2003). Satellite observations of magnetic fields due to ocean tidal flow. *Science*, *299*, 239–241.
- Vance, S., Bouffard, M., Choukroun, M., & Sotin, C. (2014, Jun). Ganymedes internal structure including thermodynamics of magnesium sulfate oceans in contact with ice. *Planetary and Space Science*, *96*, 62–70. Retrieved from <http://dx.doi.org/10.1016/j.pss.2014.03.011> doi: 10.1016/j.pss.2014.03.011
- Vance, S., & Goodman, J. (2009a). Europa. In R. T. P. W. B. M. K. Khurana (Ed.), (p. 459-482). Arizona University Press.
- Vance, S., & Goodman, J. C. (2009b). Oceanography of an ice-covered moon. In R. T. Pappalardo, W. B. McKinnon, & K. K. Khurana (Eds.), *Europa* (p. 459-482). Tucson: University of Arizona Press.
- Vance, S. D., Hand, K. P., & Pappalardo, R. T. (2016, May). Geophysical controls of chemical disequilibria in Europa. *Geophysical Research Letters*, *43*(10), 4871–4879. Retrieved from <http://dx.doi.org/10.1002/2016GL068547> doi: 10.1002/2016gl068547
- Vance, S. D., Panning, M. P., Stähler, S., Cammarano, F., Bills, B. G., Tobie, G., ... et al. (2018, Nov). Geophysical investigations of habitability in ice-covered ocean worlds. *Journal of Geophysical Research: Planets*. Retrieved from <http://dx.doi.org/10.1002/2017JE005341> doi: 10.1002/2017je005341
- Wicht, J. (2002). Inner-core conductivity in numerical dynamo simulations. *Phys. Earth Planet. Int.*, *132*, 281–302.
- Zimmer, C., Khurana, K. K., & Kivelson, M. G. (2000). Subsurface oceans on Europa and Callisto: Constraints from Galileo magnetometer observations. *Icarus*, *147*(2), 329–347.
- Zolotov, M. (2008). Oceanic composition on europa: Constraints from mineral solubilities. In *Lunar and planetary institute science conference abstracts* (Vol. 39, p. 2349).
- Zolotov, M. Y., & Kargel, J. (2009). On the chemical composition of Europa's icy shell, ocean, and underlying rocks. *Europa, edited by RT Pappalardo, WB McKinnon, and K. Khurana, University of Arizona Press, Tucson, AZ*, 431–458.